J Mar Sci Technol (2013) 18:358–369
DOI 10.1007/s00773-013-0213-6

ORIGINAL ARTICLE

An experimental investigation by towing tank on VIV of a long flexible cylinder for deepwater riser application

Jijun Gu · Marcelo Vitola · Jairo Coelho · Waldir Pinto · Menglan Duan · Carlos Levi

Received: 30 August 2012 / Accepted: 28 January 2013 / Published online: 17 February 2013

Abstract In this study, the dynamic response of a vertical flexible cylinder vibrating at low mode numbers with combined $x-y$ motion was investigated in a towing tank. The uniform flow was simulated by towing the flexible cylinder along the tank in still water; therefore, the turbulence intensity of the free flow was negligible in obtaining more reliable results. A lower branch of dominant frequencies with micro vibration amplitude was found in both cross-flow and in-line directions. This justifiable discrepancy was likely caused by an initial lock-in. The maximum attainable amplitude, modal analysis and $x-y$ trajectory in cross-flow and in-line directions are reported here and compared with previous literature, along with some good agreements and different observations that were obtained from the study. Drag and lift coefficients are also evaluated by making use of a generalized integral transform technique approach, yielding an alternative method to study fluid force acting upon a flexible cylinder.

Keywords Model test · Towing tank · Flexible cylinder · VIV · Integral transform

J. Gu (✉) · M. Vitola · C. Levi
Ocean Engineering Program, COPPE, Federal University of Rio de Janeiro, CP 68508, Rio de Janeiro 21941-972, Brazil
e-mail: carson817@gmail.com; gu@lts.coppe.ufrj.br

J. Coelho · W. Pinto
School of Engineering, Federal University of Rio Grande, Campus Carreiros, Rio Grande, RS 96201-900, Brazil

M. Duan
Offshore Oil/Gas Research Center, China University of Petroleum, Beijing 102249, China

1 Introduction

Vortex-induced vibration (VIV) is a major concern in the design of offshore structures, such as platforms [1, 2] and riser systems [3], since it can result in large amplitude responses of both in-line (IL) and cross-flow (CF) directions, and potentially lead to the accumulation of fatigue damage within a relatively short period of time [4, 5]. Reviews from Sarpkaya [6], Williamson and Govardhan [7] summarized recent fundamental results and discoveries with a focus on the importance of mass and damping, the concept of critical mass, the attainable amplitude, and so on.

To understand VIV, much work has already been done using numerical simulations [8, 9] or model tests [10–13]. The model tests have to be conducted if the analytical techniques fail to predict the expected behavior of the prototype, either within the tolerances required or within the confidence level required for good design. During the last 20 years, the inherent nature of VIV has been largely studied via the laboratory model tests using a spring-mounted rigid cylinder in CF motion only or in both IL and CF motions. These hydrodynamic coefficients on spring-mounted rigid cylinders are used to guide the design of long flexible structures in offshore application. However, the direct application of these hydrodynamic coefficients to offshore engineering is still under examination, since long flexible structures normally suffer high mode vibrations. Consequently, current numerical predictions for the VIV of long flexible cylinders are not accurate by several simulators (see the work by Chaplin et al. [14]).

In order to obtain hydrodynamic coefficients and understand the behavior of long flexible structures in more realistic conditions, the model tests of long flexible risers or pipelines were conducted in recent years [4, 9, 15–18].

Among the reported data were CF and IL amplitudes, $x-y$ trajectories and phase synchronization, lift and drag coefficients, dominant frequencies and modal amplitude. In an extended study, the VIV of a tandem and side-by-side arrangement of two flexible cylinders was also evaluated [19, 20]. The differences in observation between the previous and new tests of spring-mounted rigid and long flexible cylinders, such as the maximum attainable amplitudes caused by the intrinsic nature of the long flexible structures and its capacity to vibrate at high mode numbers, have been presented and were obviously helpful in guiding the design of structures such as risers or a long cylinder.

The present experimental study aimed at evaluating the dynamic response of a pinned-pinned flexible cylinder in a towing tank. Our main findings included a lower branch of frequency ratio, the different ratios of frequency (f_y/f_n, f_x/f_n), the maximum attainable amplitude, ratios between the cross-flow and the in-line motion, and the successful application of GITT to evaluate fluid force, all of which can supplement the recorded results with alternative scenarios and ultimately improve comprehensive understanding of VIV relative to long flexible cylinders.

The main findings of the present study were as follows: (1) the uniform flow was simulated by towing the flexible cylinder (with the aspect ratio 74.4) along the tank in still water, and therefore the turbulence intensity of the free flow was considered negligible in order to obtain more reliable results. (2) A lower branch of frequency ratio was captured both in CF and IL motions; this justifiable discrepancy was caused by initial lock-in. (3) Drag and lift coefficients were evaluated by making use of a generalized integral transform technique approach, yielding an alternative method for studying fluid force acting upon a flexible cylinder. In addition, several observations, such as the ratios of frequency, maximum attainable amplitude, ratios between the cross-flow and the in-line motions, were different from the results published by the previous literature. These new results will benefit future experimental and numerical work in this area.

2 Experimental details

The experiments were carried out in a towing tank, with a test section 0.75 m in width, 0.72 m in height and 16 m in length, at the School of Engineering, Federal University of Rio Grande (FURG), Rio Grande do Sul, Brazil. The uniform flow was simulated by towing the cylinder along the tank in still water, and the waiting interval was approximately 10 min between runs to avoid the influence of turbulence. The experiments were repeated three times for each combination of towing speed and top tension. Then the data were analyzed, revealing a high degree of repeatability. The current velocity ranged from 0.10 to 0.98 m/s, with approximate increments of 0.04 m/s. This range of speeds corresponds to Reynolds numbers from 1950 to 19110.

The sketch of the experimental setup is shown in Fig. 1. The flexible cylinder had an outer diameter of 19.5 mm and was constructed of plastic tube with a 6.4 mm steel core, as shown in Fig. 1a. Several nylon pieces were used to clamp the steel core and support the outer plastic tube, as shown in Fig. 1b. The instrumented flexible cylinder was pinned at both ends with two universal joints so the flexible cylinder could oscillate in both an IL direction and CF direction. The effective cylinder length was 1.45 m, with 0.7 m below the water surface. The water coverage was 48.3 % and therefore drag and lift forces could not be exerted on the full length of the cylinder. However, Chaplin et al. [15] verified that when water coverage is higher than a threshold of 30 %, the excited modes in the response will not change. A similar setup has been reported in the literature [17–20].

Strain gages were mounted on the flexible cylinder to measure the responses at five locations (identified as S1, S2, S3, S4 and S5), with the relative positions 0.84, 0.67, 0.50, 0.33, and 0.16 in length from the bottom end, respectively. At each location, four strain gages were placed as shown in Fig. 1a. The two strain gages in the x-direction were used to measure the IL vibrations, while the other two gages in the y-direction were used to measure the CF vibrations. The signals from the strain gages were calibrated with a position sensor to guarantee the accuracy of the response. Two hot films were placed horizontally behind the S4 and S5 strain gage stations to measure the wake oscillating frequency. The structural damping ratio in the air, calculated from a decay test, was found to be 3.18 %.

The natural frequency of the flexible cylinder with variable top tension was measured from plunk tests in still water. In order to find the experimental natural frequencies, the cylinder model was excited at its middle span after establishing each amount of top tension. Table 1 shows the fundamental natural frequencies in terms of different applied top tension values. Since the aspect ratio ($L/D \approx 74$) is not large, the natural frequency of the second mode was not captured.

The summary of the experiments is displayed in Table 2. The mass ratio is defined as $m^* = m/m_a$, where m denotes the cylinder model mass, and m_a denotes added mass; aspect ratio is defined as L/D; reduced velocity is defined as $U_r = V/f_n\ D$, V denotes the flow velocity; Reynolds number is defined as $Re = \rho\ V\ D/\mu$, ρ and μ denote density and viscosity of the flow, which were corrected for temperature. These main parameters of the present experimental setup are different from those of

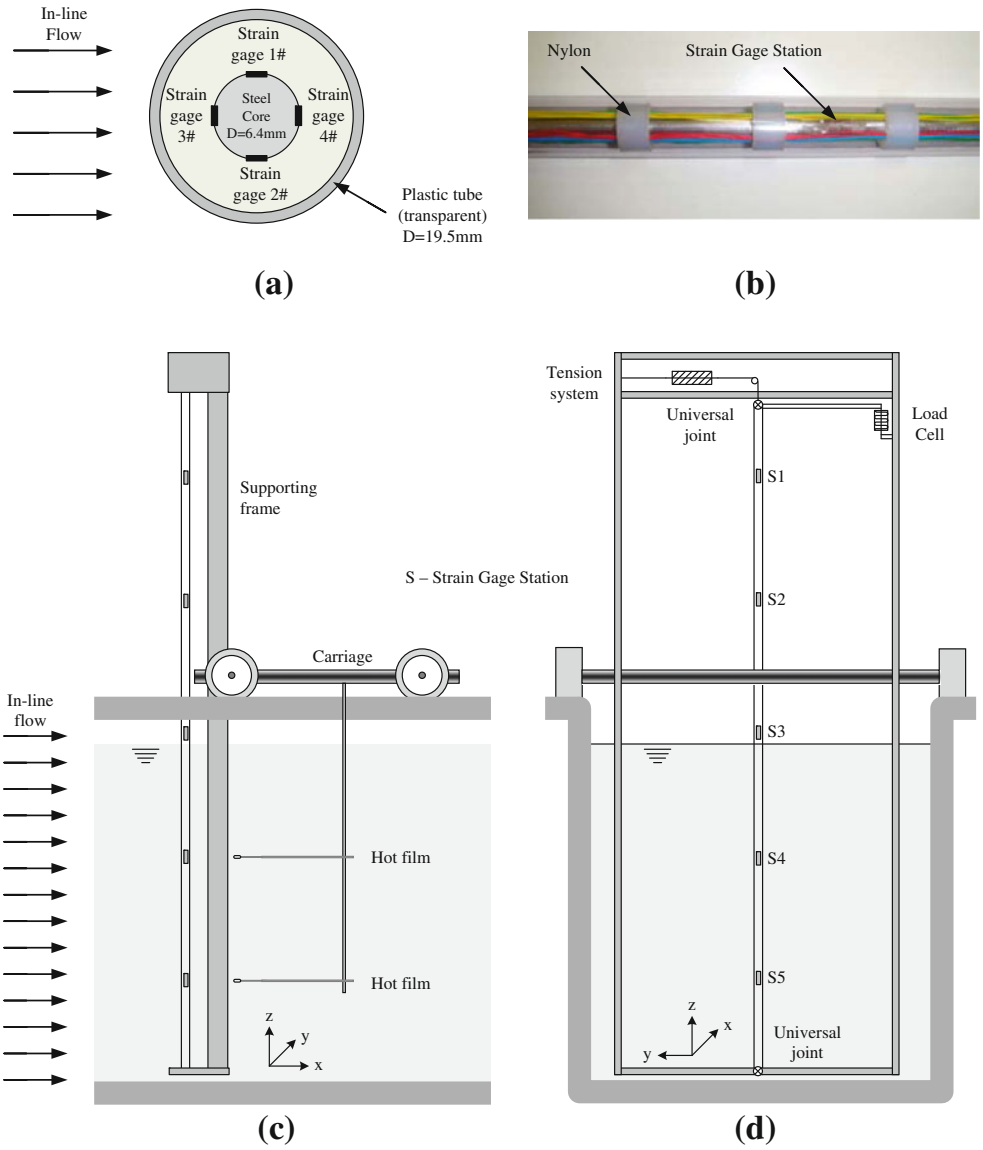

Fig. 1 Sketch of the experiment set-up. **a** Cross-section view of cylinder; **b** cylinder model; **c** side view; **d** front view

Table 1 Summary of main parameters of the experiment

Top tension T(N)	Symbol	f_n
19.6	□	4.5
29.4	○	4.83
49.0	△	5.33
68.6	+	5.67
88.2	∗	6.0
107.8	×	6.3

Table 2 Summary of main parameters of the experiment

Experiment parameters	Symbol	Unit	Value
Total length	L	m	1.45
Outer diameter	D	m	0.0195
Submerged length	L_s	m	0.70
Bending stiffness	EI	Nm^2	20.4
Mass ratio	m^*	–	1.55
Aspect ratio	Λ	–	74.4
Top tension	T_{top}	N	19.6–107.8
Flow velocity	V	m/s	0.1–0.98
Reduced velocity	U_r	–	0–12
Reynolds number	Re	–	1950–19110
Structural damping	ζ	%	3.18
Mass damping parameter	$(m^* + C_A)\zeta$	–	0.081

Huera-Huarte and Bearman [17, 18, 20], and Huera-Huarte and Gharib [19] even though they have similar aspect ratios of flexible cylinders. In addition, the towing tank used in the present study could improve the raw data quality. The

experimental results shown in this paper have some new findings and can obviously benefit future numerical and experimental studies.

3 Results and discussion

3.1 Dynamic response

The typical CF and IL time histories and the response frequencies are shown in Figs. 2 and 3 respectively, at $T_{top} = 29.4$ N, $V = 0.50$ m/s, $U_r = 4.8$, Re = 9750. The first column graph shows the time history of CF displacement in diameter for a complete run at each station of strain gage along the cylinder. The second column graph shows the time history in a time interval $t \in [15,17]$ s. The third column graph shows the spectral analysis of each signal without mean. As shown in the first column, the carriage would accelerate for approximately 5 s to achieve stable velocity. The second column graph demonstrates a stable instantaneous displacement. As shown in the third column, only one peak of vibration frequency appeared in the CF spectral analysis, whereas two peaks are captured in the IL spectral analysis, which reveal that the IL vibration captured the second mode in addition to the first.

The second mode was not achieved in the IL response for all test cases. Figure 4 shows the spectral analysis of the midpoint displacement with respect to different values of reduced velocity and applied top tension at midpoint. The right column graph reveals that when the reduced velocity is higher than about 3.5, the second mode of IL response appears. However, the spectral power of the first mode is larger than that of second mode in most of the cases, which means IL responses are still dominated by the first mode. The reason should be that at such a low aspect ratio (74.4), the cylinder model is more like a beam rather than a string. The bending stiffness plays a more important role in this dynamic vibration, which yields a higher natural frequency when compared with Huera-Huarte [21], whose aspect ratio reaches 470. As Huera-Huarte and Bearman [17] explained, with a lower aspect ratio, the frequency of IL excitation force should be high enough to reach the natural frequency of the second mode, which happened more easily in some cases with higher flow velocity and lower top tension. This is confirmed by the right column of Fig. 4 , which demonstrates that the second mode of IL response starts to be excited at a higher Reynolds number with higher top tension.

The ratios of dominant IL (f_x), CF (f_y) frequency and wake oscillating frequency (f_h) versus natural frequency (f_n) are shown in Fig. 5. The lock-in region of reduced velocity from 4.5 to 8 is clearly observed in Fig. 5. The linear fitting is implemented in all plots. The slope of the linear fitting of the CF ratio (f_y/f_n) is 0.18, as shown in Fig. 5b; and the slopes of two linear fittings of the IL ratio (f_x/f_n) are 0.18 and 0.36, respectively, as shown in Fig. 5a. These ratios are higher than that published by Huera-Huarte and Bearman [17] who observed the slopes 0.16 and 0.32, as shown in Fig. 6.

The CF ratio (f_y/f_n) is 0.23 (solid line with slope = 0.23) when reduced velocity is lower than 4; this value is close to the 0.22 value found by Khalak and Williamson [22, 23]. When reduced velocity is higher than 4.5, the CF ratio (f_y/f_n) should reflect unity if added mass is constant, but it departs from unity (solid line with slope = 0.0) in the lock-in region, as shown in Fig. 5b. The reason should be the

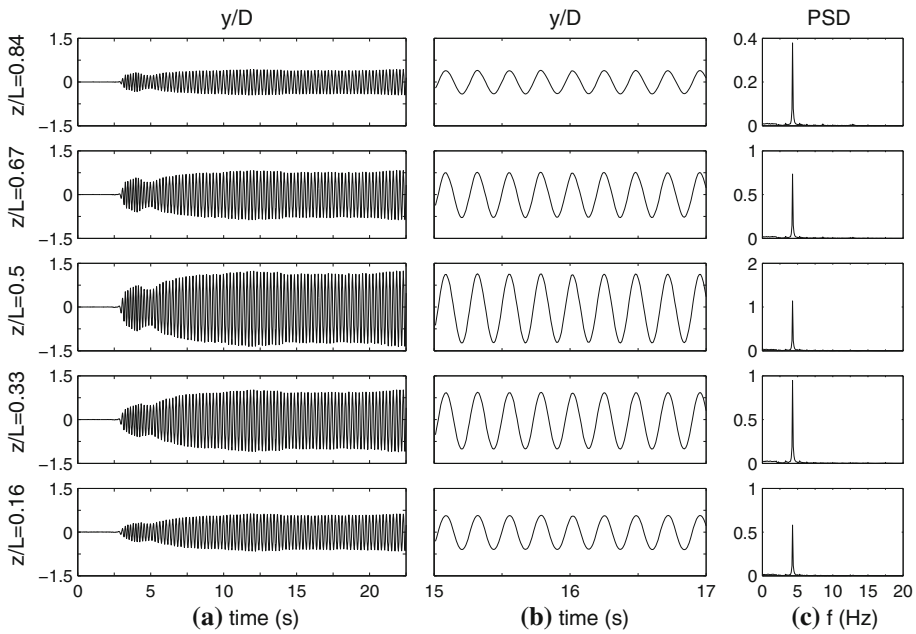

Fig. 2 Time history of test at $T_{top} = 29.4$ N, $V = 0.50$ m/s, $U_r = 4.8$, Re = 9750. **a** Time history of CF displacement in diameter of the whole run at each strain gage along the cylinder, **b** time history in an interval $t \in [15, 17]$ s, **c** spectral analysis of each signal without mean

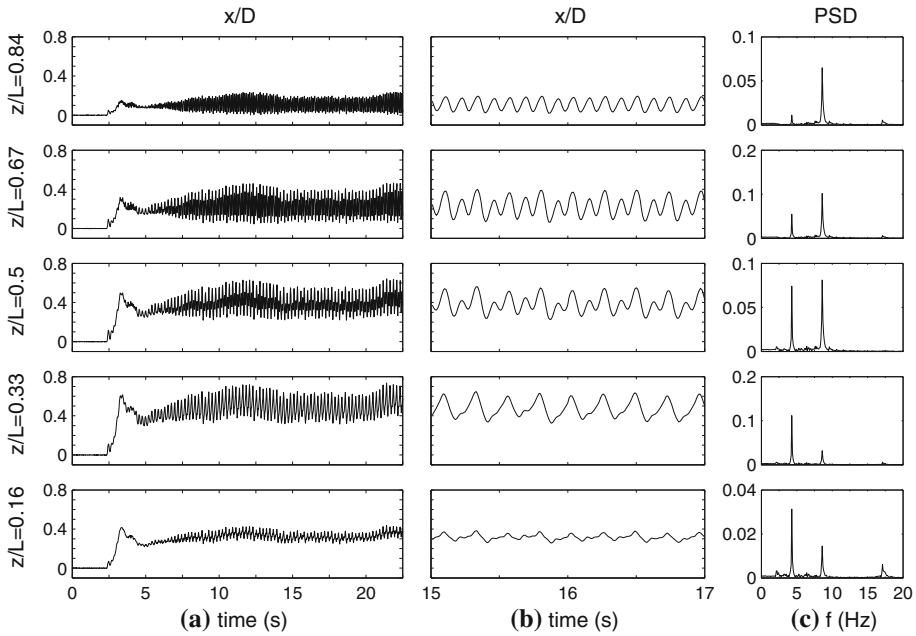

Fig. 3 Time history of test at $T_{top} = 29.4$ N, $V = 0.50$ m/s, $U_r = 4.8$, $Re = 9750$. **a** Time history of IL displacement in diameter of the whole run at each strain gage along the cylinder, **b** time history in an interval $t \in [15, 17]$ s, **c** spectral analysis of each signal without mean

low mass ratio of 1.55 found in the present study. Under low mass ratio conditions, added mass would play a more important role (see Sarpkaya [24]). Khalak and Williamson [22, 23] observed a similar phenomenon with the transverse oscillations of an elastically mounted rigid cylinder at a low mass ratio. The influence of added mass on the natural frequency was studied by Vikestad et al. [25] and the results showed that the added mass coefficient decreased from 4.5 to −1 when the reduced velocity increased from 2 to 14. The definition of reduced velocity was based on the value of the natural frequency measured in still water, which is the same as the present study. From the classical beam theory, the actual natural frequency f_n'. at the first mode of a pinned-pinned beam is defined as

$$f_n' = \frac{\pi}{2L^2}\sqrt{\frac{EI}{m + C_a m}} \tag{1}$$

where C_a denotes added mass coefficient. The natural frequency will increase when added mass coefficient decreases based on Eq. 1. When lock-in happens, the vortex shedding frequency f_y will be locked on the actual natural frequency f_n'.

The right column of Fig. 4 illustrates that a dominant frequency appears more obviously at higher top tension in the IL response when the CF lock-in has not been widely developed ($U_r < 4.5$), formatting a lower branch as shown in Fig. 5a. When CF and IL suffer lock-in ($U_r > 4.5$), these lower branch vibration frequencies disappear. The ratio of this lower branch is around 1.25. The same lower branch appeared in Fig. 6 as reported by Huera-Huarte and Bearman [17], but they did not comment on it since this value was not as remarkable as in the present study. This lower branch can also be found in the CF vibration, as shown in Fig. 5b. According to the experiment by Khalak and Williamson [22], at low mass and damping the lower branch should be induced by initial lock-in (where $U_r < 4.5$). Figure 7 depicts typical IL and CF time histories from a test in the interval $t \in [20\ 25]$ s at $T_{top} = 68.6$ N, where flow velocity is $V = 0.18$ m/s, $V = 0.22$ m/s, $V = 0.26$ m/s, respectively. The blue lines represent IL vibration and red lines represent CF vibration. The spectral analyses in the second and third columns reveal that CF vibration is composed of vortex shedding action and initial lock-in at $U_r < 4.5$, whereas IL vibration only suffers initial lock-in. The first column of Fig. 7 shows vibration amplitudes of IL and CF motions in diameters; these values are so small that the vibrations are not easily observed in experiments.

By extracting the vibration frequency from the hot films, the ratio (f_h/f_n) between wake oscillating and natural frequency is obtained and plotted as shown in Fig. 5c. The trend is very similar with the CF ratio (f_y/f_n) and the solid line has a same slope of value 0.23. However, the hot films only capture one dominant frequency, hence no lower branch is observed. When $U_r > 8$, the ratio (f_h/f_n) jumps to the solid line, which means the vibration of the flexible cylinder departs from the lock-in region. This is confirmed by Fig. 5b, where the ratio f_y/f_n becomes scattered when $U_r > 8$.

One of the most popular questions about VIV phenomena asks: what would be the maximum attainable amplitude? Figure 8 shows a compilation of the maximum CF amplitude in diameter versus the reduced velocity with various top tensions in the first row, as well as the

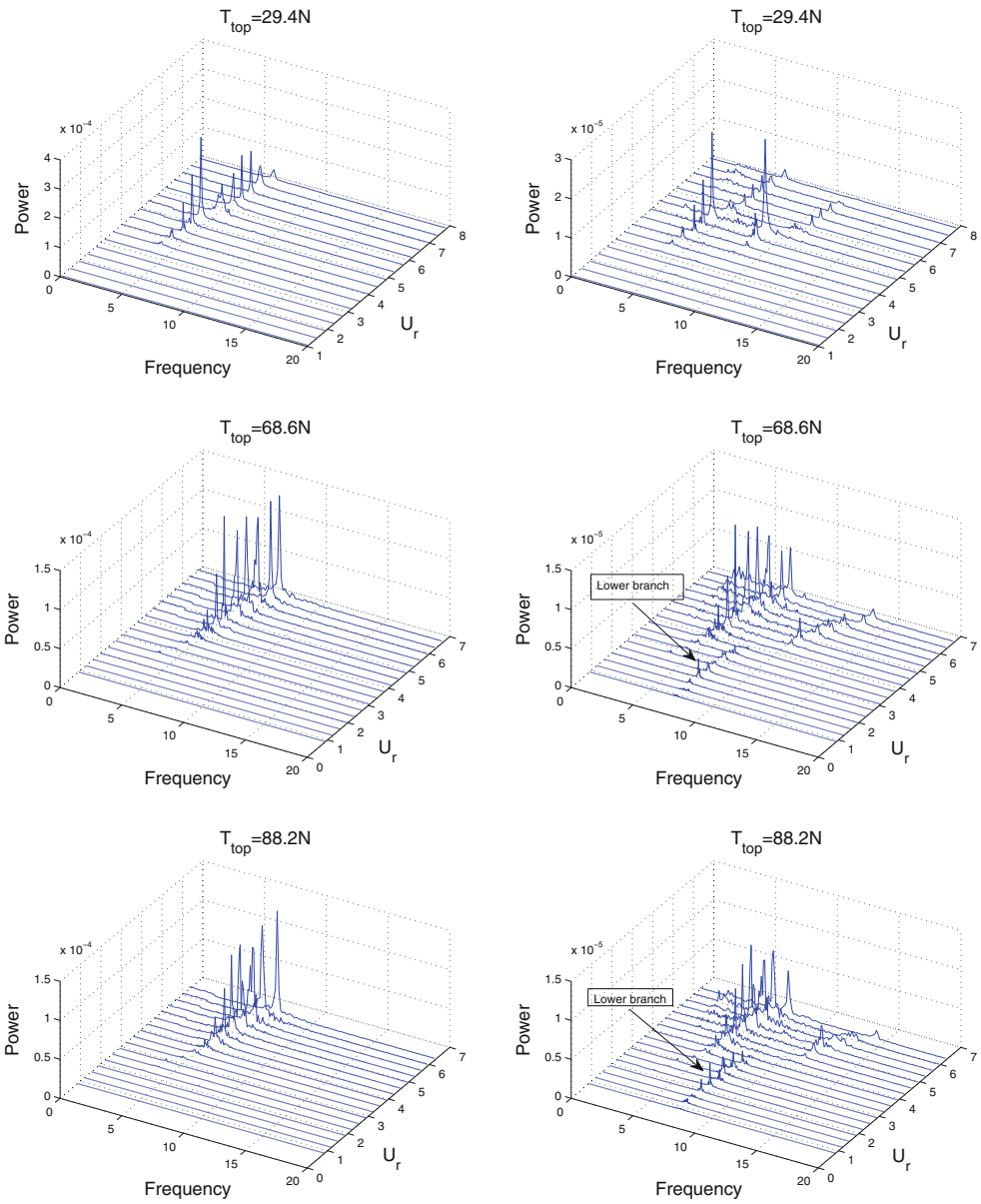

Fig. 4 Spectral analysis of the midpoint displacement at strain gage station S3. *Left graphs* CF spectral analysis; *right graphs* IL spectral analysis

maximum IL amplitude without mean in the second row. The results from Huera-Huarte [21], Huera-Huarte and Bearman [17] have been compiled and compared with the present data. The larger aspect ratio (470) experiments were performed by Huera-Huarte [21] in which the CF response could be excited to the second mode in the reduced velocity range $U_r \in [0–12]$. Hence, the maximum CF amplitude increased initially from $U_r \in [0–7.5]$, and then changed to the second mode suddenly. Afterwards, the amplitude increased from $U_r \simeq 7.5$ onward, until it arrived at the third mode. The largest CF amplitude was 1.02 in the present reduced velocity range $U_r \in [0–12]$ from Huera-Huarte [21], as shown in the figure.

Due to the similar experimental setup between the present and Huera-Huarte and Bearman [17] studies, both have a clear initial upper branch and lower branch of maxima amplitudes. For the present cases, the maxima CF amplitudes are distributed in the reduced velocity range $U_r \in [5\ 6.5]$, the maximum CF amplitude in diameter is 1.33, larger than 1.02 as reported by Huera-Huarte and Gharib [19], 0.98 from Huera-Huarte and Bearman [20] and 0.7 from Huera-Huarte and Bearman [17]. As for the IL maximum amplitude without mean, the value for the present experiment is 0.2 in diameter, which is less than 0.22 from Huera-Huarte and Bearman [17] and much less than 0.37 from Huera-Huarte [21]. The ratio between the cross-flow and the in-line motion is 6.6 for the present study, which is obviously higher than the result of 2–4 from Huera-Huarte [21]. This ratio is a basic characteristic of long flexible cylinders as mentioned by Jauvtis and Williamson [26].

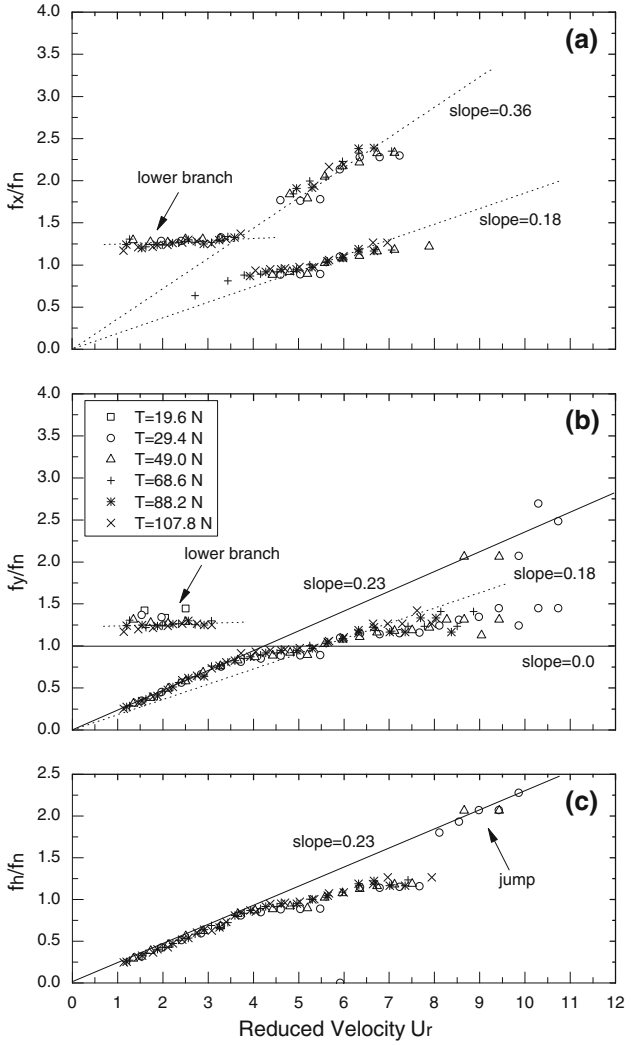

Fig. 5 Normalized IL (f_x/f_n), CF (f_y/f_n) frequencies and wake oscillating frequency (f_h/f_n) as a function of reduced velocity U_r

If a beam is governed dominantly by top tension, the response behavior then appears more like a string and the multi-mode response will be clearly shown, as in the experiments conducted by Chaplin et al. [15] and Trim et al. [4]. The second mode will be more easily reached when the top tension is lower because of the lower natural frequency. In the case of the top tension 19.6 N, the maxima amplitudes increased if reduced velocity was above 8.5, in both CF and IL directions. This means that the excited response would approach the second mode slightly. Modal analysis has been widely used to identify different modes of vibration; this methodology can be found in the previous literature [16]. By applying modal analysis here, mode numbers (up to 3) have been chosen to separate the original response into each mode weight contribution, as shown in Fig. 9. The figure of mode weights indicates that in all cases they have been dominated by the first mode in both CF and IL responses. The

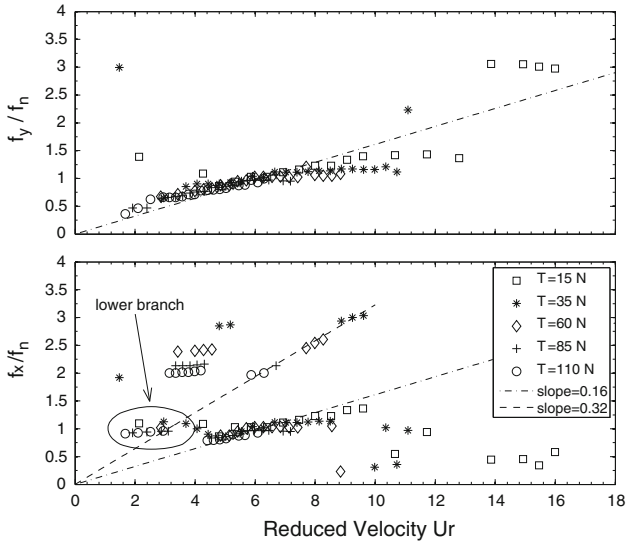

Fig. 6 Normalized IL (f_x/f_n), CF (f_y/f_n) frequencies as a function of reduced velocity U_r. From Huera-Huarte and Bearman [17]

second mode only appears weakly in the CF and IL responses if reduced velocity ranges from $U_r \in [5\,6]$ as depicted in the second row. The third mode has almost no contribution to the overall response. The present result has a good agreement with Huera-Huarte [21].

Figure 10 shows the instantaneous $x-y$ trajectories versus the reduced velocity at each strain gage station. The case of $T_{\text{top}} = 29.4$ N, $U_r = 5.3$ is clearly exhibited in a figure-8 pattern at $z/D = 0.84, 0.67, 0.5$. Figure 11 indicates the instantaneous deflections in CF and IL directions in a time interval $t \in [8\,14]\,s$ at $T_{\text{top}} = 29.4$ N, $U_r = 5.3$ m/s corresponding to the case in the third column of Fig. 10. The left column is the instantaneous CF deflection, the middle column is the IL deflection and the third column is the IL deflection without mean. In all cases, the IL mean displacements at $z/D = 0.33$ are larger than the ones at $z/D = 0.84$; this is confirmed by the second column in Fig. 11, due to: (1) the drag force in water is much higher than in air, hence larger drag force exerts on the lower half of the flexible cylinder; (2) lower axial tension force acts on the lower half of the flexible cylinder due to its weight.

An important question in investigating the VIV phenomenon is in regards to the attainable amplitude in CF direction. A log-log plot was used by Griffin [27] for attainable amplitude A^* versus mass damping ($m^*\zeta$), which could collapse peak amplitude data. Using a large set of experimental data from elastically mounted cylinders, Khalak and Williamson [23] plotted attainable amplitude A^* versus $(m^* + C_A)\zeta$ and a successful collapse of the data appeared in the upper and the lower branches. For the present data, $(m^* + C_A)\zeta = 0.081$, attainable amplitude is $A^* = 1.33$. A compilation of data including comparison with results from the literatures [17, 19–21, 23, 27, 28] is

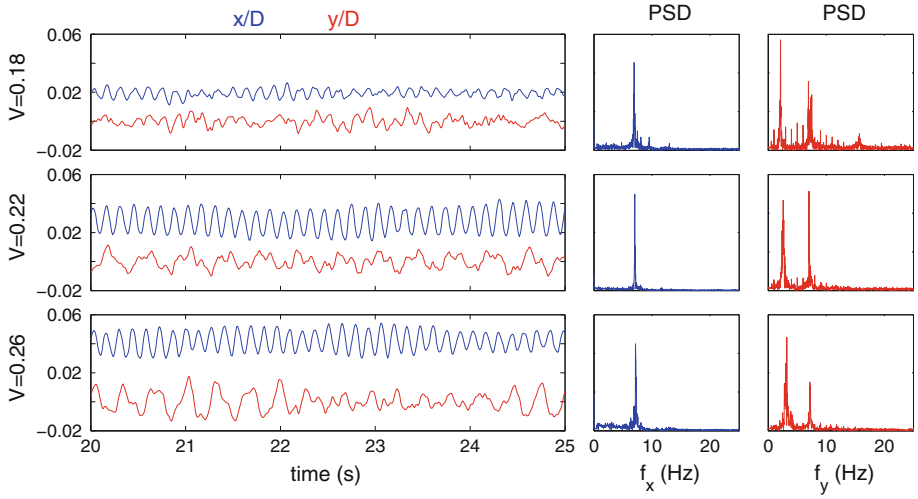

Fig. 7 Time history and spectral analysis of tests at $T_{top} = 68.6$ N. *First column* time history of a test in the interval $t \in [20\,25]\,s$; *second column* spectral analysis of IL vibration; *third column* spectral analysis of CF vibration. *First row* $V = 0.18$ m/s, $U_r = 1.63$; *second row* $V = 0.22$ m/s, $U_r = 1.99$; *third row* $V = 0.26$ m/s, $U_r = 2.35$

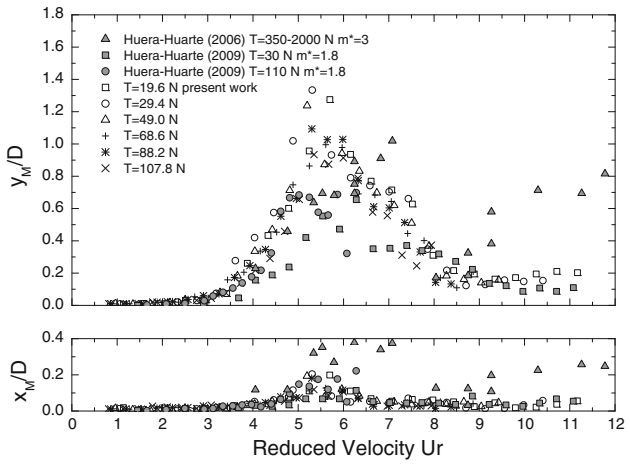

Fig. 8 The maximum IL (x_M/D) and CF displacements (y_M/D)

shown in Fig. 12. From the figure, it is evident that the attainable amplitudes in $x-y$ motion with pinned-pinned flexible cylinders are somewhat larger than those with spring-mounted cylinders. For instance, the attainable amplitude could reach the range $A^* = 1.0$–1.6 from Huera-Huarte [21], and $A^* \backsimeq 1.0$ from Huera-Huarte and Bearman [20], Huera-Huarte and Gharib [19], both of which are larger than most of the cases with spring-mounted cylinders. The present result $A^* = 1.33$ also confirms such a trend.

3.2 Drag and lift coefficient

The drag and lift coefficients are dimensionless coefficients that relate the fluid force acting on a reference area associated with the body, which are defined as:

$$C_D = \frac{F_D}{\frac{1}{2}\rho V^2 D}, \qquad C_L = \frac{F_L}{\frac{1}{2}\rho V^2 D}, \tag{2}$$

where F_D and F_L are drag and lift forces per unit submerged length, acting perpendicularly to the axis of the cylinder.

The drag and lift coefficients of a spring-mounted rigid cylinder have been largely estimated in the literature [22, 28], but they have not been well evaluated for a pinned-pinned flexible cylinder. A finite element method model (FEM) was used by Huera-Huarte et al. [29] to obtain the instantaneous distributed in-line and transverse forces acting on a flexible cylinder, but this still resulted in an approximation due to use of the stiffness, mass and damping matrices, which are not updated with each time step. Hence, an alternative method, the generalized integral transform technique (GITT), has been used to obtain fluid force. The methodology can be found in Cotta [30] and Gu et al. [31], and a brief introduction will be shown here, assuming a dimensionless governing equation of dynamic response of a flexible cylinder with a pinned-pinned boundary condition as:

$$\frac{\partial^2 y(z,t)}{\partial t^2} + \delta\frac{\partial y(z,t)}{\partial t} - c\frac{\partial^2 y(z,t)}{\partial z^2} + b\frac{\partial^4 y(z,t)}{\partial z^4} = f(z,t), \tag{3}$$

with the following boundary conditions:

$$y(0,t) = 0, \quad \frac{\partial^2 y(0,t)}{\partial z^2} = 0, \quad y(1,t) = 0, \quad \frac{\partial^2 y(1,t)}{\partial z^2} = 0, \tag{4}$$

where δ, c, b denote damping, tension and flexural stiffness characteristics. Following the ideas in the GITT, the eigenvalue problems for transverse displacement $y(z, t)$ is given by:

$$\frac{d^4\phi_i(z)}{dz^4} = \lambda_i^4\phi_i(z), \quad 0 < z < 1, \tag{5}$$

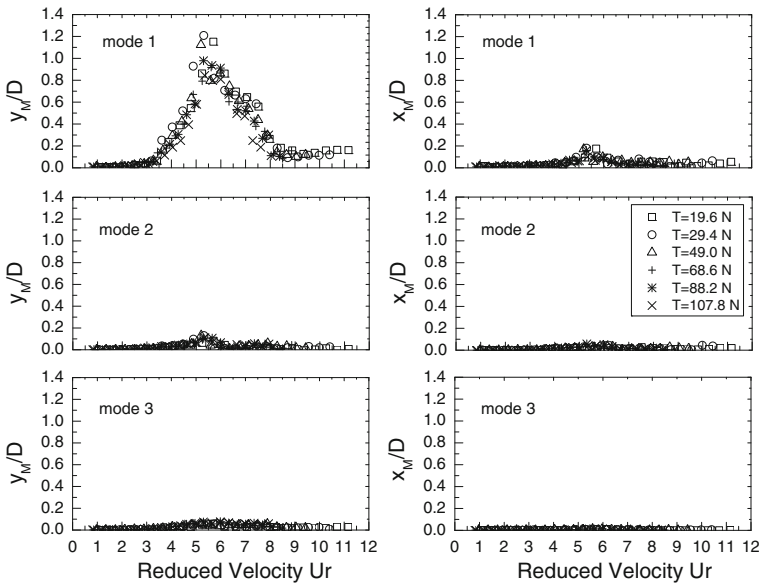

Fig. 9 Modal weights: CF (*left*) and IL (*right*) oscillations up to the third mode

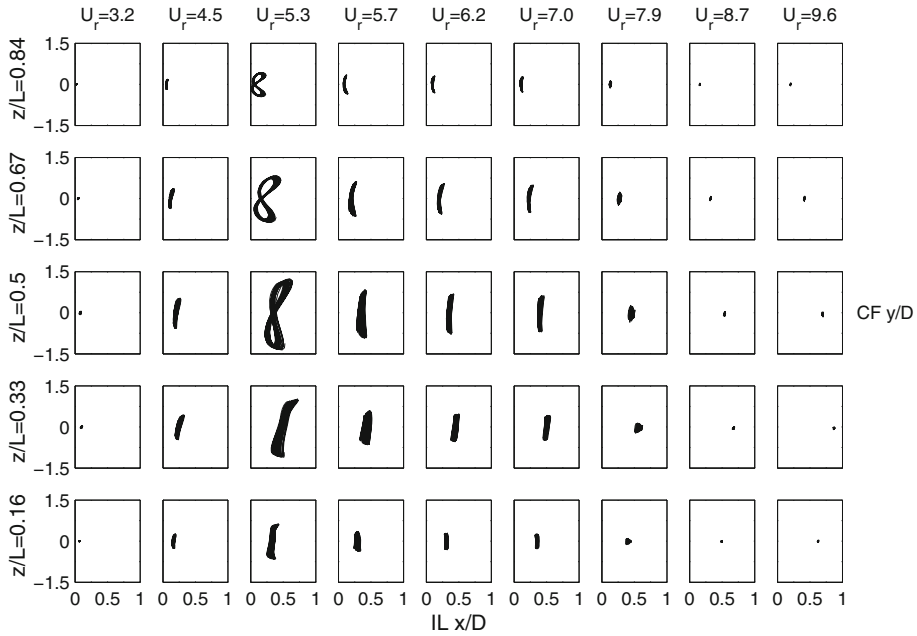

Fig. 10 IL and CF trajectories at different reduced velocities U_r and $T_{top} = 29.4$

where λ is eigenvalue. The eigenfunction satisfies the following orthogonal property:

$$\int_0^1 \phi_i(z)\phi_j(z)\mathrm{d}z = \eta_{ij}N_i, \tag{6}$$

with $\eta_{ij} = 0$ for $i \neq j$, and $\eta_{ij} = 1$ for $i = j$. The eigenvalue problem shown in Eq. 5 allows definition of the following integral transform pairs:

$$\begin{cases} \bar{y}_i(t) = \int_0^1 \tilde{\phi}_i(z)y(z,t)\mathrm{d}z, & \text{transform}, \\ y(z,t) = \sum_{i=1}^{\infty} \tilde{\phi}_i(z)\bar{y}_i(t), & \text{inversion}, \end{cases} \tag{7a, b}$$

$$\begin{cases} \bar{f}_i(t) = \int_0^1 \tilde{\phi}_i(z)f(z,t)\mathrm{d}z, & \text{transform}, \\ f(z,t) = \sum_{i=1}^{\infty} \tilde{\phi}_i(z)\bar{f}_i(t), & \text{inversion}, \end{cases} \tag{8a, b}$$

To perform the integral transform process, the dimensionless Eq. 3 is multiplied by the operator $\int_0^1 \tilde{\phi}_i(z)\mathrm{d}z$, the inverse formula 7b and 8b are applied, yielding, after some mathematical manipulations, the following set of ordinary differential equations:

$$\frac{\mathrm{d}^2\bar{y}_i(t)}{\mathrm{d}t^2} + \delta\frac{\mathrm{d}\bar{y}_i(t)}{\mathrm{d}t} - c\sum_{j=1}^{\infty}\tilde{P}_{ij}\bar{y}_j(t) + b\lambda_i^4\bar{y}_i(t) = \bar{f}_i(t), \quad i = 1, 2, 3, \ldots, \tag{9}$$

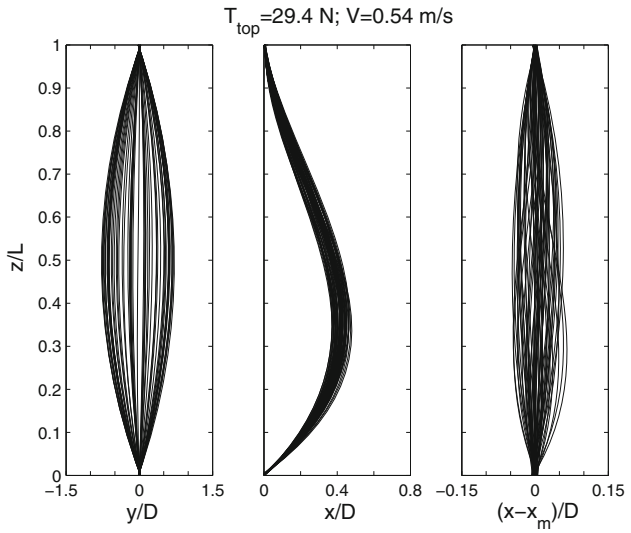

Fig. 11 Instantaneous deflections: (1) *Left column graph* the instantaneous CF deflection; (2) *middle column graph* IL deflection; (3) *right column graph* IL deflection without mean. *Black lines* plotted at every 0.1 s in the time interval $t \in [8\ 14]$ s, $T_{\text{top}} = 29.4$ N, $V = 0.54$ m/s, $U_{\text{r}} = 5.3$

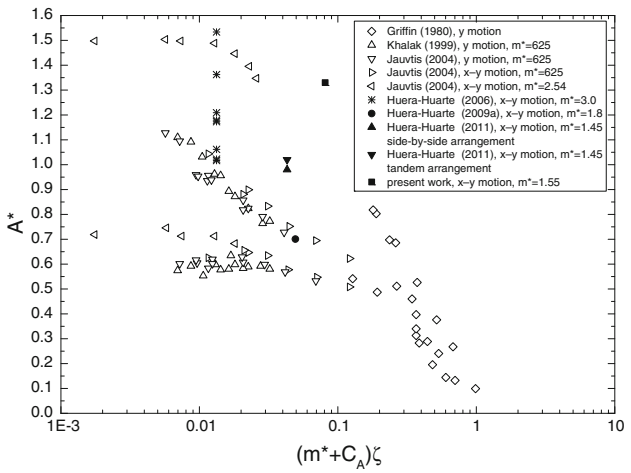

Fig. 12 Peak amplitude data

where the coefficient $\tilde{P}$ is analytically determined from the following integral:

$$\tilde{P}_{ij} = \int_0^1 \tilde{\phi}_i(z) \frac{\mathrm{d}^2 \tilde{\phi}_j(z)}{\mathrm{d}z^2} \mathrm{d}z. \tag{10}$$

$\frac{\mathrm{d}^2 \bar{y}_i(t)}{\mathrm{d}t^2}$, $\frac{\mathrm{d}\bar{y}_i(t)}{\mathrm{d}t}$ and $\bar{y}_j(t)$ can be obtained by the integration of Eq. 7b; once $\bar{f}_i(t)$ has been numerically evaluated, the analytical inversion formula 7b recovers the dimensionless function $f(z, t)$.

Figure 13 depicts a compilation of mean drag coefficients, including the present experimental results based on GITT and those based on FEM from Huera-Huarte and Bearman [18]. It is noticed that the drag coefficient increases from 1.7 to 3.5 when U_{r} increases from 0 to 5.5, and then decreases from 3.5 to 1.7 when $U_{\text{r}} = 5.5$ onwards. This trend agrees well with the results from Huera-Huarte and Bearman [18]; moreover, the results of this study present a better feature, which is not as scattered as that of Huera-Huarte and Bearman [18]. The reason could be the towing tank does not have the influence of turbulence.

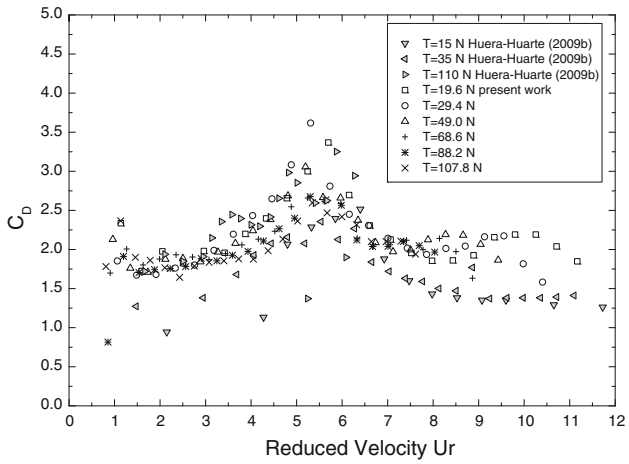

Fig. 13 Mean drag coefficients

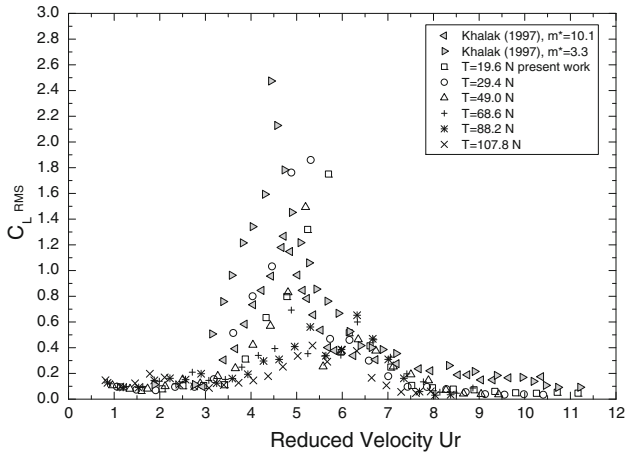

Fig. 14 Root mean square (RMS): lift coefficients

Since GITT results can represent the drag coefficient successfully, the RMS of the lift coefficient can also be obtained, as shown in Fig. 14. Previous experimental results based on a spring-mounted cylinder [22] are compared to the present results. From the figure, $C_{\text{L RMS}}$ increases monotonically before the transition (in the range $U_{\text{r}} \in [0\ 5.5]$). After the transition, it decreases rapidly (in the range $U_{\text{r}} \in [5.5\ 12]$), thus yielding very clear upper and lower branches as maximum displacement. These upper and lower branches agree well with Khalak and Williamson [22].

4 Conclusions

With this study, we aimed to improve an understanding of the vortex-induced vibration behavior of a long flexible cylinder for deepwater riser application. Comparisons between the present data and results from literature have been shown. The following new findings and conclusions can be drawn:

1. The present setup successfully simulated VIV phenomena and captured several useful characteristics of VIV. The slope of the linear fitting of the CF ratio (f_y/f_n) was 0.18. The two slopes associated with the IL ratio (f_x/f_n) were 0.18 and 0.36, respectively. A lower branch was captured both in CF and IL motions; this justifiable discrepancy was caused by initial lock-in.
2. The maximum attainable amplitude was 1.33 diameters in the CF direction, and 0.2 diameters in the IL direction. The ratio between the cross-flow and the in-line motion was 6.6, which was obviously higher than the value of 2–4 from Huera-Huarte [21].
3. The $x-y$ trajectory plot indicated that the figure-8 patterns could only be found in a few cases. The 'Griffin' plot was used to show that the present result $A^* = 1.33$ was higher than the results found in the experiments with a spring-mounted cylinder at the same range of $(m^* + C_A)\zeta$.
4. Drag and lift coefficients were evaluated based on GITT solutions, and comparison with previous results were performed to show their reliability and capability. This method could be an alternative numerical tool to evaluate the fluid force of the long flexible structures.

These new observations are obviously different from the results published in the literature [17–21], the main reasons being the different characteristics of the riser model and experimental setup. The Reynolds numbers of the present experiment were small, since it is very difficult to reach realistic Reynolds numbers in laboratory experiments due to limitations of size and technical characteristics of the facilities. In addition to the main governing parameter, the Reynolds number for the dynamic response of circular cylinders, other influencing parameters such as turbulence intensity, aspect ratio, bending stiffness, mass damping parameter and applied top tension can also affect dynamic response. The accuracy of the present experimental setup ensures that the new observations are reliable and confident. The main findings, including the differences of the frequency ratios (f_y/f_n, f_x/f_n), the maximum attainable amplitude, ratios between the cross-flow and the in-line motion, and the successful application of GITT to evaluate fluid force, illustrate the effectiveness of the present study and are helpful in guiding the design of structures such as risers or a long cylinder.

Acknowledgments The author would like to thank the Brazilian National Research Council (CNPq) and the National Basic Research Program of China (973 Program) Grant No. 2011CB013702 for financial support of this research.

References

1. Rodolfo T, Goncalves, Andre LC Fujarra, Guilherme F Rosetti, Kazuo Nishimoto (2009) Mitigation of vortex-induced motion, (VIM) on a monocolumn platform: forces and movements. J Offshore Mech Arctic Eng Trans ASME, 132(4). 28th international conference on ocean, offshore and arctic engineering, Honolulu
2. Rosetti GF, Goncalves RT, Fujarra ALC, Nishimoto K (2011) Parametric analysis of a phenomenological model for vortex-induced motions of monocolumn platforms. J Br Soc Mech Sci Eng 33(2):139–146
3. Pesce CP, Martins CD, da Silveira LMY (2004) Riser–soil interaction: local dynamics at TDP and a discussion on the eigenvalue and the VIV problems. J Offshore Mech Arctic Eng Trans ASME 128(1):39–55. 23rd international conference on offshore mechanics and arctic engineering (ASME), Vancouver
4. Trim AD, Braaten H, Lie H, Tognarelli MA (2005) Experimental investigation of vortex-induced vibration of long marine risers. J Fluids Struct 21(3):335–361
5. Gao Y, Zong Z, Sun L (2011) Numerical prediction of fatigue damage in steel catenary riser due to vortex-induced vibration. J Hydrodyn 23(2):154–163
6. Sarpkaya T (2004) A critical review of the intrinsic nature of vortex-induced vibrations. J Fluids Struct 19(4):389–447
7. Williamson CHK, Govardhan R (2004) Vortex-induced vibrations. Annu Rev Fluid Mech 36:413–455
8. Yamamoto CT, Meneghini JR, Saltara F, Fregonesi RA, Ferrari JA (2004) Numerical simulations of vortex-induced vibration on flexible cylinders. J Fluids Struct 19(4):467–489
9. Jung D, Kim H, Shin (2012) Characteristics of VIV in multi-degree-of-freedom tensioned beams using a numerical method. J Mar Sci Technol 9:1–11
10. Pesce CP, Fujarra ALC (1998) Vortex-induced vibrations and jump phenomenon: experiments with a clamped flexible cylinder in water. Int J Offshore Polar Eng 10(1):26–33. 8th international offshore and polar engineering conference (ISOPE-98), Montreal
11. Yang B, Gao FP, Jeng DS, Wu YX (2008) Experimental study of vortex-induced vibrations of a pipeline near an erodible sandy seabed. Ocean Eng 35(3–4):301–309
12. Yang B, Gao FP, Wu YX (2008) Flow-induced vibrations of a cylinder with two degrees of freedom near rigid plane boundary. Int J Offshore Polar Eng 18(4):302–307
13. Nishi Y, Ono K, Kokubun K (2012) Development of a renewable energy system utilizing vortex induced vibration of a cylinder and principle of leverage aiming for application in deep sea. J Mar Sci Technol, 1–8
14. Chaplin JR, Bearman PW, Cheng Y, Fontaine E, Graham JMR, Herfjord K, Huera-Huarte FJ, Isherwood M, Lambrakos K, Larsen CM, Meneghini JR, Moe G, Pattenden R, Triantafyllo MS, Willden RHJ (2005) Blind predictions of laboratory measurements of vortex-induced vibrations of a tension riser. J Fluids Struct 21(1):25–40
15. Chaplin JR, Bearman PW, Huera-Huarte FJ, Pattenden RJ (2005) Laboratory measurements of vortex-induced vibrations of a vertical tension riser in a stepped current. J Fluids Struct 21(1):3–24
16. Lie H, Kaasen KE (2006) Modal analysis of measurements from a large-scale VIV model test of a riser in linearly sheared flow. J Fluids Struct 22(4):557–575

17. Huera-Huarte FJ, Bearman PW (2009) Wake structures and vortex-induced vibrations of along flexible cylinder-part 1: dynamic response. J Fluids Struct 25(6):969–990
18. Huera-Huarte FJ, Bearman PW (2009) Wake structures and vortex-induced vibrations of along flexible cylinder-part 2: drag coefficients and vortex modes. J Fluids Struct 25(6):991–1006
19. Huera-Huarte FJ, Gharib M (2011) Flow-induced vibrations of a side-by-side arrangement of two flexible circular cylinders. J Fluids Struct 27(3):354–366
20. Huera-Huarte FJ, Bearman PW (2011) Vortex and wake-induced vibrations of a tandem arrangement of two flexible circular cylinders with near wake interference. J Fluids Struct 27(2):193–211
21. Huera-Huarte FJ (2006) Multi-mode vortex-Induced vibrations of a flexible circular cylinder. PhD thesis, Imperial College London, London
22. Khalak A, Williamson CHK (1997) Fluid forces and dynamics of a hydroelastic structure with very low mass and damping. J Fluids Struct 11(8):973–982
23. Khalak A, Williamson CHK (1999) Motions, forces and mode transitions in vortex-induced vibrations at low mass-damping. J Fluids Struct 13(7–8):813–851
24. Sarpkaya T (1979) Vortex-induced oscillations: a selective review. J Appl Mech 46(2):241–258
25. Vikestad K, Vandiver JK, Larsen CM (2000) Added mass and oscillation frequency for a circular cylinder subjected to vortex-induced vibrations and external disturbance. J Fluids Struct 14(7):1071–1088
26. Jauvtis N, Williamson CHK (2003) Vortex-induced vibration of a cylinder with two degrees of freedom. J Fluids Struct 17(7): 1035–1042
27. Griffin OM (1980) Vortex-excited cross-flow vibrations of a single cylindrical tube. J Pressure Vessel Technol Trans ASME 102(2):158–166
28. Jauvtis N, Williamson CHK (2004) The effect of two degrees of freedom on vortex-induced vibration at low mass and damping. J Fluid Mech 509:23–62
29. Huera-Huarte FJ, Bearman PW, Chaplin JR (2006) On the force distribution along the axis of a flexible circular cylinder undergoing multi-mode vortex-induced vibrations. J Fluids Struct 22(6–7):897–903
30. Cotta RM (1998) The integral transform method in thermal and fluids sciences and engineering. Begell House, New York
31. Gu J, An C, Duan M, Levi C, Su J (2013) Integral transform solutions of dynamic response of a clamped-clamped pipe conveying fluid. Nucl Eng Design 254:237–245